Nanostructure of mouse otoconia

Dimitra Athanasiadou[a], Wenge Jiang[a,1], Natalie Reznikov[b], Alejandro B. Rodríguez-Navarro[c], Roland Kröger[d], Matthew Bilton[e], Alicia González-Segura[f], Yongfeng Hu[g], Valentin Nelea[a], Marc D. McKee[a,h*]

[a]Faculty of Dentistry, McGill University, Montreal, QC, Canada H3A 0C7

[b]Object Research Systems Inc., Montreal, QC, Canada H3C 1M4

[c]Departamento de Mineralogía y Petrología, Universidad de Granada, Granada, Spain 18002

[d]Department of Physics, University of York, York, UK YO10 5DD

[e] Imaging Centre at Liverpool, University of Liverpool, Liverpool, UK L69 3GL

[f]Centro de Instrumentación Científica, Universidad de Granada, Granada, Spain 18002

[g]Canadian Light Source, University of Saskatchewan, Saskatoon, SK, Canada S7N 2V3

[h]Department of Anatomy and Cell Biology, McGill University, Montreal, QC, Canada H3A 0C7

***Corresponding author**

Email address: Prof. Marc D. McKee marc.mckee@mcgill.ca

[1]Present address: Department of Chemistry, Tianjin Key Laboratory of Molecular Optoelectronic Sciences, and Tianjin Collaborative Innovation Center of Chemical Science & Engineering, Tianjin University, Tianjin, P. R. China, 300072.

Abstract

Mammalian otoconia of the inner-ear vestibular apparatus are calcium carbonate (calcite)-containing mineralized structures critical in maintaining balance and in detecting linear acceleration. The mineral phase of otoconia coherently diffracts X-rays much like single-crystal calcite. Among mineral-associated proteins, otoconia contain osteopontin (OPN) – a highly phosphorylated mineral-binding protein influencing mineralization processes in bones, teeth and avian eggshells. Here, we investigate mineral structure and OPN distribution in mouse otoconia at the ultrastructural level. Scanning electron and atomic force microscopy of intact mouse otoconia and otoconia cleaved open using a microtome revealed an internal nanostructure (averaging 50-nm Feret diameters). Further investigation by transmission electron microscopy and electron tomography of focused ion beam-prepared sections of otoconia confirmed this mineral nanostructure, and identified even smaller (approximately 10 nm) nanograin dimensions. X-ray diffraction identified only calcite mineral in the otoconia, and Raman and X-ray absorption spectroscopy – both methods being sensitive to the detection of crystalline and amorphous forms in the sample – showed no evidence of amorphous calcium carbonate in the otoconia. Scanning and transmission electron microscopy combined with colloidal-gold immunolabeling for OPN revealed that this protein was located at the surface of the otoconia, correlating with a site where surface nanostructure was observed. OPN addition to calcite growing *in vitro* produced similar surface nanostructure. Finally, these findings provide details on the composition and nanostructure of mammalian otoconia, and suggest that while OPN may influence surface rounding and surface nanostructure in otoconia, other incorporated proteins (also possibly including OPN) likely participate in creating internal nanostructure.

Keywords: Biomineralization; otoconia; osteopontin; calcite; nanostructure; tomography

1. Introduction

Biomineralization processes have been broadly studied for many mineralized tissues and structures (Lowenstam and Weiner, 1989). Otoconia (and otoliths in fish) are composites of calcium carbonate ($CaCO_3$) mineral and proteins found in the utricle and the saccule of the vestibular apparatus of vertebrate mammals, and in the lagena of nonmammalian vertebrates (Hiatt, 2014; Lundberg et al., 2015). The vestibular system of the inner ear is responsible for head movement detection, for spatial orientation, and for body balance (Hiatt, 2014; Marieb, 1991). In mammals, the vestibular system has three fluid-filled semicircular canals which respond to rotational acceleration, and two receptor organs – the utricle and the saccule – which sense linear acceleration and gravity (Hughes et al., 2006; Lundberg, 2012; Lundberg et al., 2015).

Otoconia are formed in mammals during the late embryonic stages, and they are considered stable until mid-life where signs of their degeneration can be detected in humans (Anniko et al., 1984). In mice – which share many similar otoconial features to humans – the initial seeding of otoconia is detected at embryonic day 14, with the highest rate of mineralization occurring at embryonic days 15 and 16 (Ornitz et al., 1998). Murine otoconia acquire their final size (a few micrometers) by postnatal day 7, and from there, in health, they generally are preserved throughout life with minimal changes/transitions (House and Honrubia, 2003; Ornitz et al., 1998). Otoconia, surrounded by a low-calcium solution termed the endolymph, are embedded in a membranous structure called the otoconial membrane, which rests on the extremities of hair cell kinocilia and stereocilia in the utricular and saccular sensory epithelium, regions known as the macula (Lundberg, 2012; Lundberg et al., 2015). With each head movement, the otoconia are displaced by their moments of inertia relative to the underlying cells, leading to bending of the sensory hair bundles (Lundberg, 2012). This mechanical impetus is transformed to electrical signals that are

transmitted by the hair cells to the central nervous system of the brain, providing information on the spatial position of the head (Lundberg, 2012; Marieb, 1991).

Morphologically, mammalian otoconia are barrel-shaped calcitic structures bounded by well-defined rhombohedral facets at both ends and which diffract as single crystals (Lundberg, 2012). They are unique in being the only calcium carbonate-containing biomineral found in normal healthy mammals; the main mineral phase of bones and teeth is a calcium phosphate (apatite). However, in some species, calcium phosphate otoconia can be found such as in the *Agnatha* species (jawless fish) where there is negligible or absent crystalline structure (Carlstrom, 1963), or in malformed human inner ears where a mixture of apatite and calcite has been reported (Johnsson et al., 1982). Otoconia can occur as any of the $CaCO_3$ polymorphs depending upon the organism within which they reside (Ross and Pote, 1984). In mammals and birds, the polymorph for otoconia is typically calcite, the most thermodynamically stable calcium carbonate polymorph existing under ambient conditions (Lins et al., 2000). In amphibians and fish, the predominant polymorph is aragonite (Carlstrom, 1963; Ross and Pote, 1984). Vaterite is found in primitive jawfish or in pathologic conditions in the human inner ear (Addadi et al., 2003; Johnsson et al., 1982; Ross and Pote, 1984; Wright et al., 1982). Specific matrix proteins have been shown to promote the calcium carbonate polymorph selection of otoconia (Pote and Ross, 1991).

As in other biominerals, and important for the $CaCO_3$ formation in the inner ear, is the presence of an organic matrix consisting mainly of glycoproteins and proteoglycans (Fermin et al., 1995; Lundberg, 2012; Lundberg et al., 2015; Pote and Ross, 1993; Tachibana and Morioka, 1992). The presence of otoconial proteins is necessary for the formation of otoconia where they sequester and concentrate calcium ions from the endolymph fluid (Lundberg, 2012), likely amongst other important functions in guiding otoconial growth. Prominent proteins identified in

mammalian otoconia are otoconin 90 (OC90), otolin-1 (or otolin), osteopontin (OPN), fetuin-A, SPARC-like protein 1 (SC1), secreted protein acidic and rich in cysteine (SPARC), dentin matrix protein 1 (DMP1) (Lundberg, 2012; Lundberg et al., 2015; Thalmann et al., 2006) and α-tectorin (Xu et al., 2010). OC90 – the main soluble matrix protein of otoconia – modulates the form of calcite crystals *in vitro* (Lu et al., 2010), whereas *in vivo* in mice, in the absence of this protein, there is either an absence of otoconia, or only a few massive abnormal otoconia are formed, with overall calcite amounts being decreased roughly by half (Andrade et al., 2012; Xu et al., 2010). Otolin – identified in bony fish (Murayama et al., 2005) – is a member of the collagen X family, and is found in both otoconia and the surrounding otoconial matrix where it might serve as a scaffold protein for biomineralization (Moreland et al., 2014; Yang et al., 2011). Other proteins such as fetuin-A, SPARC, OPN and DMP1, are considered as minor otoconins because of there being a negligible phenotype effect on otoconial formation and vestibular function in transgenic mice (Xu et al., 2010; Zhao et al., 2007; Zhao et al., 2008). Other candidates for mediating otoconial mineralization are the keratan sulfate proteoglycans (KSPGs) (Xu et al., 2010), these being extended biomolecules having strong negative charges for attracting calcium ions and appearing to interact with OC90 and otolin proteins (Lundberg, 2012).

OPN is a highly phosphorylated mineral-binding protein, having multiple roles in cell adhesion and protein binding in the extracellular matrix of bone and teeth, where the phosphoserine residues and the overall negative charge of this molecule elicited from Asp and Glu residues appear to be important for regulating mineralization processes (Fisher et al., 2001; Sodek et al., 2000; Sorensen et al., 1995). OPN is expressed by the sensory hair cells, the nonsensory dark cells, and the cells of the endolymph sac (Zhao et al., 2008). In recent work pertaining to OPN and biomineralization in another calcium carbonate structure – the avian eggshell – we have shown an

association of OPN with the nanostructured texture of the calcitic shell, and we have reproduced similar internal nanostructure in calcite crystals grown *in vitro* in the presence of OPN (Athanasiadou et al. 2018).

Structural studies of mammalian otoconia are sparse, and those that exist mainly describe pathologic circumstances and developmental abnormalities (Johnsson et al., 1982; Wright et al., 1982). In terms of their ultrastructure, human otoconia are known to be composed of three sectors/branches at each end that extend outwards from the central so-called belly region, a site seemingly more susceptible to otoconial degradation (Walther et al., 2014). Despite having both rounded and faceted external morphology at the microscale suggesting perhaps nonclassical crystallization pathways (De Yoreo et al., 2015; Rodriguez-Navarro et al., 2016; Wolf et al., 2016), it remains possible that an internal polycrystalline, coherent nanostructure forms during their formation in the presence of mineral and calcium-binding proteins, as has been shown in numerous calcium-carbonate mineralizing systems (Athanasiadou et al., 2018; Jean-Pierre Cuif, 2010; Tseng et al., 2014).

Morphological and compositional alterations of otoconia are frequently produced by head trauma, ototoxic drugs, aging, and environmental and genetic factors, and these can lead to balance-related disorders (Lundberg et al., 2015). Benign paroxysmal positional vertigo (BPPV) is a serious disease in which patients suffer from intense nausea and loss of balance (Salvinelli et al., 2004). BPPV occurs when otoconia are dislodged from their initial position and migrate into the semicircular canals (canalithiasis), or when otoconia exist in larger numbers than the active surface area of the utricular cells (utriculithiasis) (Oas, 2001). Aging-related otoconial degeneration is a high-risk factor for creating free otoconial debris that results in loss of balance

in elderly people, consequently leading to falls which frequently cause bone fractures and even death (Agrawal, 2009).

Because of the important physiologic functions effected by otoconia, and because otoconial pathologies lead to BPPV, accurate and detailed knowledge of the formation of otoconia and their fine structure is fundamental to understanding the function of the vestibular system. Given the limited understanding of otoconial formation and structure, and to better consider ways to influence their regrowth/regeneration to potentially treat their abnormalities, we describe here the internal structure of mouse otoconia at the nanoscale level. We also describe the localization of OPN at the ultrastructural level in these otoconia, and combine this with an examination of the *in vitro* effects of OPN on growing calcite morphology.

2. Materials and Methods

2.1 Harvesting and embedding of otoconia

Otoconia were processed by manual dissection under a stereomicroscope from C57BL/6 normal (wild-type) and *Opn*$^{-/-}$ (knockout) mice obtained from the Jackson Laboratory (Bar Harbor, ME, USA). All mice used were 8 days old (except for those used for the 2D XRD and EBSD analyses which were 3 months old, Sections 2.3 and 2.9 below). Animals were kept at 24°C in pathogen-free conditions using alternating 12-hour light and 12-hour dark cycles. Mice were fed normal mouse chow (2920X, Teklad global soy protein-free extruded rodent diet, Envigo, Huntingdon, UK), and had access to water *ad libitum*. Mice were sacrificed under isoflurane anesthesia by decapitation, and mouse heads were either fixed with aldehyde and then dissected to isolate the inner ear and dehydrated and embedded in Epon or LR White resin, or the heads were transferred unfixed immediately into 100% ethanol to prevent any potential dissolution of otoconia

from exposure to aqueous solutions. From the latter, otoconia were carefully retrieved through dissection under a stereoscope, and stored in 100% ethanol. Embedded samples were sectioned for histology and mounted on either glass slides for atomic force microscopy or onto grids for scanning electron microscopy (that were also used additionally for transmission electron microscopy). Animal procedures were evaluated and approved by the McGill University Institutional Animal Care and Use Committee following the guidelines of the Canadian Council on Animal Care.

2.2 Light microscopy of the vestibular inner ear system

For the histology of the inner ear vestibular system and observation of otoconia *in situ*, 1-µm-thick sections from wild-type mouse otoconia were cut from polymerized blocks using a Leica Ultracut E Ultramicrotome (Leica, Wetzlar, Germany). These sections were von Kossa-stained for mineral (black reaction) followed by counter-staining with toluidine blue, with visualization and image recording using an optical microscope (model DMRBE, Leica) equipped with a 3-CCD Sony DXC-950 camera (Sony, Tokyo, Japan).

2.3 X-ray diffraction (XRD), Raman spectroscopy and X-ray absorption (XAS) of the mineral phase of mouse otoconia

The mineral phase of wild-type mouse otoconia was analyzed by powder and single-crystal X-ray diffraction (XRD), Raman spectroscopy and X-ray absorption spectroscopy (XAS). Powder XRD was run on a Bruker D8 Discover diffractometer equipped with a Cu X-ray tube (wavelength 0.154056 nm) and an area detector (GADDS 2D XRD).

For XRD, measurements were performed in coupled θ-θ scan mode (500 µm beam spot size) with samples of otoconia spotted as aggregates onto a quartz sample substrate. Single-crystal XRD analyses were performed using a Bruker D8 Venture diffractometer equipped with a photon

area detector and a Cu X-ray microsource (200 μm beam size). Measurements were taken in the transmission mode on aggregates of otoconia (dissected from 3-month-old wild-type mice). Frames were recorded while the sample was rotating in φ angle within a 10° angular range using 0.3° steps and an integration time of 60 seconds.

Raman spectroscopy was performed using a Renishaw inVia Raman microscope (Renishaw, Gloucestershire, UK) equipped with a holographic spectrometer and a Leica DM2500 M optical microscope (Leica Microsystems GmbH, Wetzlar, Germany). The excitation source was a 514.5 nm Ar laser with a *ca*. 2 μm laser spot size and a 25 mW excitation power. The laser was focused through a 50× objective (numerical aperture 0.75) on a dense array of otoconia. For each measurement, Raman spectra were acquired for 10 seconds where 3 scans were accumulated for minimizing any noise effects. Spectral reproducibility was confirmed by taking several spot analyses. Measurements were done on 1-μm-thick sections of utricle cut with an ultramicrotome from Epon blocks containing sectioned otoconia and placed on glass coverslips.

XAS synchrotron data collection was performed at the Canadian Light Source (CLS) using the SXRMB beamline. Sections of resin-embedded otoconia cut at 1-μm thickness were placed onto Si wafers. The electron beam was run at 2.9 GeV with a beam current of approximately 200 mA. A set of 5 scans was averaged from three samples to achieve the best signal-to noise ratio. All spectra were obtained at the calcium K-edge and were normalized in reference to the positions of the intrinsic monochromator glitches and of the calcite edge spectrum.

2.4 Scanning electron microscopy (SEM)

To analyze by SEM both the outer surface of otoconia and the internal structure of microtome (diamond knife)-cleaved otoconia, isolated intact otoconia and resin-embedded otoconia were prepared. For external morphology examination, intact isolated whole otoconia

were placed on aluminum SEM stubs, coated with a 2-nm thick Pt layer, and examined by SEM at an accelerating voltage of either 2 or 5 kV using an Inspect F-50 FE-SEM (FEI Company). Without sputter coating, ultramicrotome-cut 1-µm-thick microtome sections of otoconia were placed on conductive grids (also for future TEM use) where likewise imaged by SEM under the same conditions.

2.5 Atomic force microscopy (AFM)

To further investigate possible internal nanogranular structure of otoconia, and to correlate this with the nanoscale distribution of organic matrix in the same sample, atomic force microscopy (AFM) was conducted on 1 µm-thick ultramicrotome cut sections from wild-type mice. AFM height and amplitude images were taken using a Multimode Nanoscope IIIa atomic force microscope (Veeco, Santa Barbara, CA, USA) operating in the tapping mode in air at room temperature using a nonvertical engage E-scanner and NanoScope version 5.30 software (Veeco/Bruker-AXS Inc., Madison, WI, USA). In the AFM experiments, V-shaped tapping mode probes (typical tip apex radius of approximately 7 nm) with Si cantilevers having a spring constant k = 42 N/m (Bruker-AXS Inc.) were used. The tip force exerted on the surface was optimized by the amplitude set-point being as high as possible to reduce imaging artefacts. The Feret diameters of the units comprising the observed nanostructure were calculated using ImageJ software (1.x version) (Schneider et al., 2012). At least 200 Feret diameters of the otoconial nanostructure domains were calculated from the AFM images (obtained in amplitude mode) after performing the software's high-pass processing to enhance domain boundaries.

2.6 Focused-ion beam (FIB) sample preparation and transmission electron microscopy (TEM)

The TEM investigation was performed on a thin FIB section of an otoconium prepared by a dual-beam FIB system (FEI Helios 600 NanoLab, FEI, Hillsboro, OR, USA) equipped with a gallium ion source. For this, a nickel TEM grid with otoconia was placed on a flat aluminium SEM stub. A single otoconium was then identified and covered with a protective 2 µm-thick Pt layer from which a 2 µm-thick slab cut from the otoconium was milled/thinned with the FIB. Afterward this initial thinning, the section was transferred onto a Cu TEM half-grid using an EasyLift nanomanipulator for the final thinning at 5 kV and 9.4 nA, from which an 80-nm-thick section was obtained. Bright-field TEM images and selected-area electron diffraction (SAED) patterns were obtained using a Tecnai TF-20 (FEI) microscope operating at 200 kV.

2.7 Electron tomography

The 80-nm-thick FIB-cut section of an otoconium collected on a TEM Cu grid was used to collect a series of single-axis tilt images at an accelerating voltage of 200 kV using a Tecnai G2 F20 cryo-S/TEM (FEI) equipped with a Gatan Ultrascan 4000 4k × 4k digital CCD camera system (model 895). Images were taken at a magnification of 62,000X over a tilt range from –40° to +50° for the samples (2° increments in both low tilts and high tilts). The resulting images had pixel sizes of 0.19 nm. For electron tomography in a scanning transmission electron microscope (STEM) (shown in Supplementary Material), images were recorded using a ThermoFisher 300 kV Titan^3 Themis X-FEG S/TEM at a magnification of 62,000 over a tilt range from –50° to +70° (2° increments in low tilts and 1° high tilt step on the 80-nm-thick sections). The images from the tilt series were aligned, filtered and reconstructed into a tomogram using the IMOD software package (Kremer et al., 1996). The movies for the raw tilt series and reconstruction were done in IMOD, whereas the movies with 3D volume with solid and surface rendering were generated using UCSF Chimera (version 1.10.1) software.

2.8 3D imaging and reconstruction

Three-dimensional imaging of intact utricular otoconia embedded in an LR White resin block was performed using a Zeiss Xradia 520 Versa (Carl Zeiss Canada Ltd). A series of X-ray frames (totalling 1989 projections) was collected over 360-degrees of rotation at 60 V with a pixel resolution of 0.5 µm. A reconstructed movie of the rotation series was generated using Dragonfly^{TM} v3.6 software (Object Research Systems Inc., Montreal).

2.9 Electron backscatter diffraction (EBSD) and pole figures

Electron backscattering diffraction (EBSD) maps were collected for 20 h from FIB-cut sections of otoconia in the transmission mode using an Auriga Zeiss SEM instrument and a 0.3 µm-step size resolution. All EBSD data were collected and analyzed with AZtec 2.1 software (Oxford Instruments). Data was visualized as crystallographic orientation maps using pseudocolors to represent crystal orientations or pole figures.

2.10 Calcite crystal growth in the presence of OPN

Synthetic calcite crystals were grown *in vitro* in a 10 mM $CaCl_2$ solution with (or without) added full-length phosphorylated bovine milk OPN (0.15, 0.3, 0.45 and 0.9 µM) as provided by Arla Foods and prepared according to the procedure described by Sørensen and Petersen (Sorensen and Petersen, 1993). Calcite crystallization took place for 2 hours on round glass coverslips in small wells placed within a sealed desiccator previously charged with 1 g of $(NH_4)_2CO_3$ powder. Glass coverslips with calcite crystals were gently removed from solution, and lightly rinsed with distilled water and ethanol, and then, air-dried and placed in a desiccator for storage until further characterization. Triplicates were used for all the crystallization experiments.

2.11 Immunogold labeling for OPN

For immunogold OPN labeling of otoconia *in situ* in normal wild-type mice and OPN-deficient mice (negative control), TEM grid-mounted microtome-cut sections 80 nm in thickness, as well as the respective polymerized block faces themselves from which the sections were cut, were used to localize OPN at the EM level. Otoconia-containing thin sections and block faces were incubated with anti-mouse OPN antibody (R&D Systems Oakville, Canada) for 1 hr followed by washing and incubation with protein A-colloidal gold complex (14-nm gold particles, from G. Posthuma, University of Utrecht) for 1 hr to detect the immunolabeling reactions. For the sections, conventional staining with uranyl acetate and lead citrate was performed after the immunolabeling protocol. The microtome-cut sections were visualised by TEM as described above, and the block faces were visualized by SEM.

3.1 Results

3.2 Optical microscopy and scanning electron microscopy (SEM) – external morphology of otoconia

Figure 1a shows by light microscopy an overview of the location of otoconia in the mouse inner ear from a von Kossa and toluidine blue-stained section of the utricle from wild-type mice. Otoconia stained black for mineral (arrow) rest upon a gelatinous mass – the otoconial membrane – overlying the hair cells of the utricular macula. Figures 1b and 1c show by SEM the external morphology of wild-type mouse otoconia at low and high magnification, respectively, while Movie S1 (Supp. Material) displays the 3D organization of otoconia in the utricle as determined from microcomputed X-ray tomography. The size of the majority of the otoconia generally ranged between 5 to 8 μm, with some smaller otoconia of approximately 2 μm in length being present

(Fig. 1b). Higher magnification of the otoconial surface reveals an external nanogranular structure on the barrel-shaped body (Fig. 1c inset), whereas the triplanar faceted surfaces appear smooth (Fig. 1c).

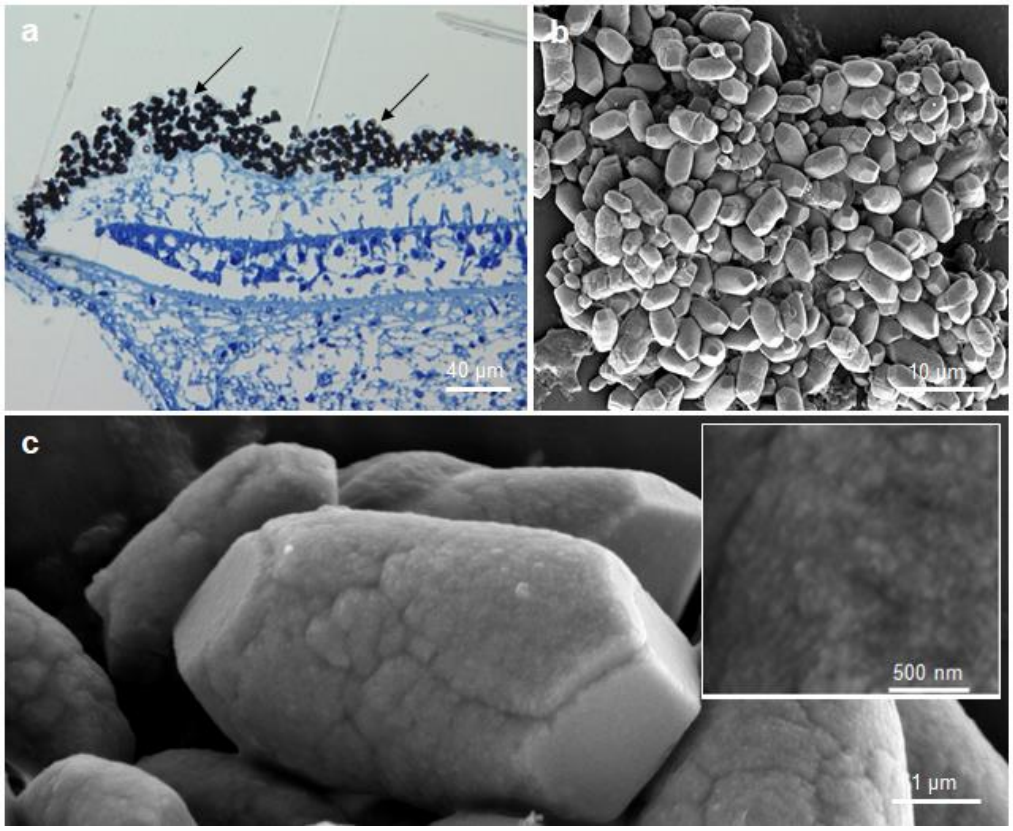

Figure 1. External morphology of wild-type mouse otoconia. (a) Histological staining of a section of the mouse utricle observed by light microscopy after von Kossa staining for mineralized otoconia (black, arrows). (b) Low-magnification SEM image of otoconia. (c) High-magnification SEM image showing details of otoconia having surface nanostructure (inset).

3.3 XRD, Raman spectroscopy and XAS – identification of $CaCO_3$ polymorphs and crystallinity of otoconia

As has been observed previously (Pote and Ross, 1986), mouse otoconia are crystallized in the form of calcite. XRD patterns from a cluster of many agglomerated otoconia revealed

306 characteristic peaks corresponding only to calcite (Fig. 2a). Similar to the XRD results, Raman
307 spectra revealed characteristic peaks in the region between 100-1200 cm^{-1} attributable to vibrations
308 arising from the calcite polymorph (Fig. 2b). Particularly demonstrating this, the bands 281 cm^{-1}
309 and 155 cm^{-1} are characteristically attributable to the vibrations of the complete unit cell, referred
310 to as lattice modes. Other bands above 400 cm^{-1} are attributable to the internal modes of the
311 carbonate ions, the symmetric stretching at 1085 cm^{-1} and the in-plane bending at 711 cm^{-1}
312 (Wehrmeister et al., 2011). No evidence of amorphous calcium carbonate was observed from 8
313 day-old mice otoconia. The pre-edge peak at 4035.8 eV, corresponding to the electronic transition
314 1s-3d being characteristic for ACC samples (Politi et al., 2006), was absent from the Ca K-edge
315 XAS spectra of the otoconia (Fig. 2c), and only crystalline forms of Ca (calcite) was present.

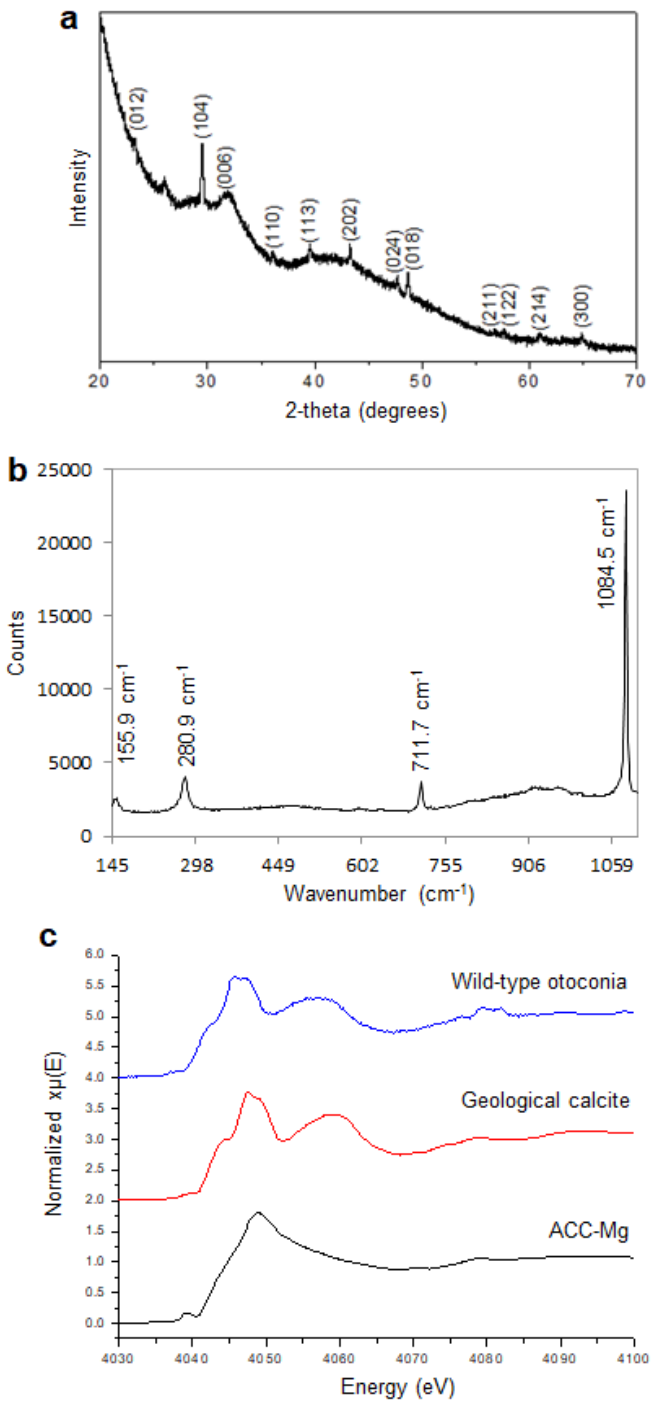

316

317 **Figure 2. Calcitic mouse otoconia.** (a) XRD pattern showing calcite as the mineral phase in
318 mouse otoconia indicating the predominant crystallographic plane reflections. (b) Raman spectrum
319 obtained from a single otoconium. The Raman spectrum was compared with spectra obtained from
320 a Raman database (http://rruff.info/). (c) XAS spectra of wild-type mouse otoconia showing peaks
321 characteristic for calcite. The spectrum was compared with XAS spectra of geological calcite and
322 ACC-Mg obtained under the same experimental imaging conditions.

3.4 Internal structure of otoconia

Figure 3a shows an SEM image of an uncoated, ultramicrotome-cut single otoconium revealing ubiquitous nanostructure throughout its interior. To further analyze and confirm this nanogranular structure, ultramicrotome-cut sections were also examined by AFM. AFM height (Fig. 3b) and amplitude (Fig. 3c) analysis revealed an aligned (inset) otoconial nanogranular structure consisting of about 50 ± 14 nm (SD) in Feret diameter. Phase-mode AFM images, as shown in Figure 3d, revealed delineating margins of different composition at the boundaries of the nanostructure (arrows). Since there was no evidence of ACC in our samples according to the XRD, Raman and XAS spectroscopy data, at this mouse age (8-day-old), these phase variations are attributed to the presence of organic content delineating the nanostructure.

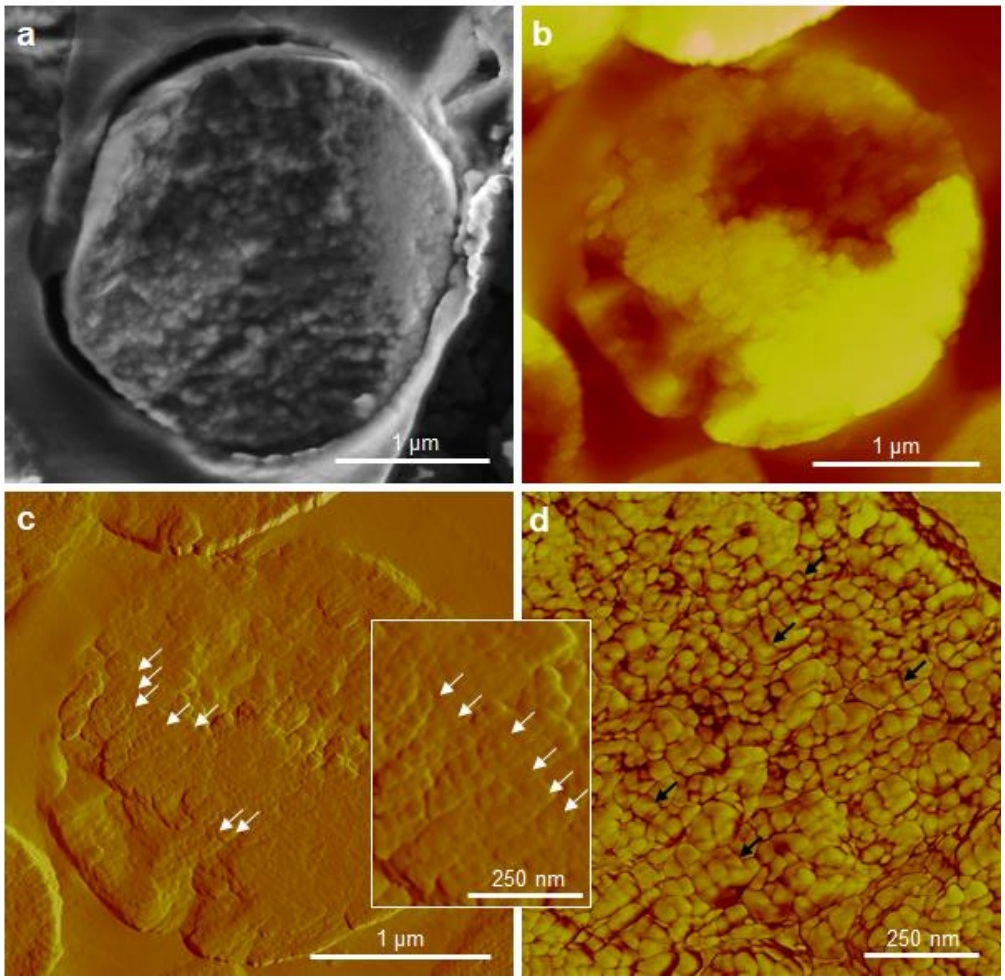

Figure 3. Interior nanostructure of wild-type mouse otoconia. (a) SEM image of the interior of an otoconia from an uncoated otoconium. AFM image in (b) height and (c) amplitude mode showing internal otoconial nanostructure. (d) AFM phase-mode image showing linear arrays of inorganic calcitic nanogranules (yellow, white arrows) surrounded by organic material (red, black arrows). Otoconia were cut/fractured open using a microtome-mounted diamond knife.

As examined by TEM, an even smaller nanostructure size of approximately 10 nm in diameter was detected as seen by higher magnification lattice imaging (Fig. 4a). SAED of these regions showed predominantly single-crystal alignment (Fig. 4a, inset), demonstrating highly coherent alignment of the nanostructured subunits. Electron tomography 3D reconstructions of mouse otoconia (Figs. 4b-d, and Supp. Material Movies S2, S3) showed abundant and homogeneously dispersed 10-nm-sized nanodomains together with the larger nanostructure initially observed and measured by AFM (Figs. 3b-d). STEM bright and high-angle annular dark-field imaging (HAADF) confirmed the nanostructure of otoconia as shown in Figures S1a,b.

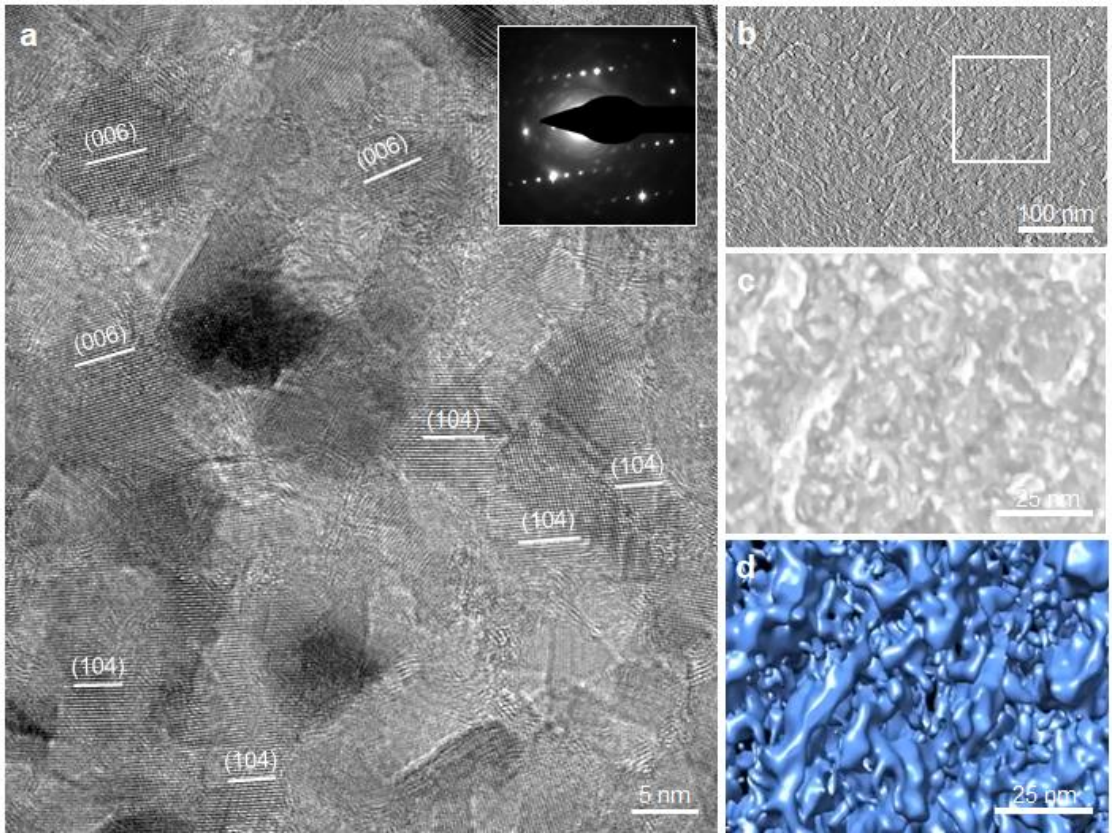

Figure 4. Nanostructure of otoconia by TEM after FIB sectioning. (a) High-resolution TEM lattice imaging of nanodomains, with SAED indicating predominantly single crystal alignment. (b) Bright-field TEM image from a tilt series of a nanostructured branch region. (c and d) Three-dimensional tomographic reconstructions of the nanodomain branch region indicated by the box in (b) [solid and surface rendering in (c) and (d), respectively].

Single-crystal 2D XRD of otoconia showed calcitic diffraction rings with rounded spots that were similar to those produced by ground geological calcite crystal (optical-quality Iceland spar) which indicate that aggregates of otoconia are generally randomly oriented with respect to each other, and that the crystalline phase of individual otoconia behaves like high-quality calcite single crystals (Figs. 5a,b). Despite this single crystal behaviour in diffraction, we observed by SEM, AFM and electron tomography an internal granular nanostructure similar to that observed in other calcium carbonate biomineralization systems. Thus, the nanograins forming the otoconia calcite crystals must have a nearly perfect coherent orientation as seen in the SAED patterns (Fig. 4a, inset). These nanograin results are supported by the data in the 001 pole figures and their contour plots obtained after whole-otoconia EBSD data analysis where the angular spread values for geological calcite and otoconia are quite low and quite similar (0.58 deg and 0.47 degrees, respectively) (Figs. 5c-f).

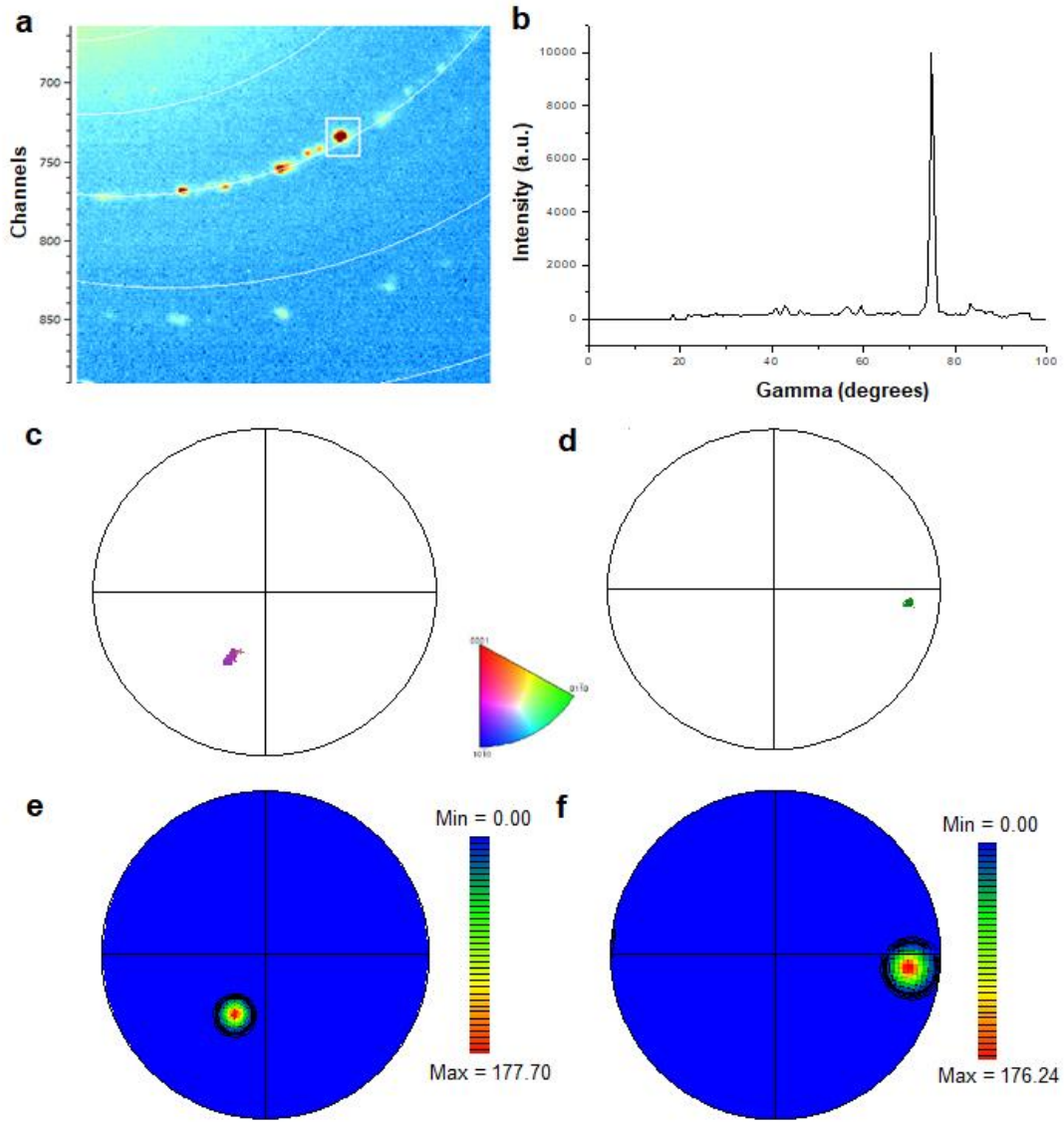

Figure 5. 2D XRD and EBSD analysis of otoconia. (a) 2D X-ray diffraction pattern produced by otoconia showing single-crystal diffraction spots (white box). (b) Intensity profile along the 104 calcite ring as a function of the γ angle. (c and d) 001 pole figures showing almost identical scattering of the *c*-axis within geological calcite and otoconia, respectively. (e and f) Contour plots of the same data shown in c and d, respectively.

3.5 Immunogold labeling for OPN in mouse otoconia

The colloidal-gold immunolabeling imaging approach was used to provide a means for high-resolution localization and mapping of proteins in mineralized tissues by electron microscopy

(McKee and Nanci, 1995). Furthermore, if samples can be cut with microtome, postembedding immunogold labeling allows protein localization within the interior of biomineralized specimens. Here, we were able to detect OPN in otoconia by both TEM and SEM in wild-type and *Opn*$^{-/-}$ mice, the latter being used as a negative control where the transgenic mice have been designed to lack entirely OPN in all their tissues, induced by intentional gene ablation approach.

OPN at the surface of the otoconia was readily detected, with Figures 6a-d showing TEM and SEM immunogold labeling for OPN as indicated in wild-type mice. As expected, no labeling was observed in negative-control mice lacking OPN (*Opn*$^{-/-}$) (Figs. 6e-h). A limiting difficulty with this approach is that the aqueous procedures necessary to do antibody labeling and other protocol steps particularly for relatively soluble calcite-containing samples, produces essentially a total decalcification of the otoconia and release of mineral-bound proteins into the solution (indeed, this is how otoconial proteins can be extracted for biochemical analyses). In the present study, this aqueous dissolution unfortunately resulted in voids in the prepared samples (all panels of Fig. 6) which precluded potential labeling of the interior of the otoconia, but allowed OPN localization at the surface of the otoconia where OPN molecules are trapped locally at the surface by the infiltrated embedding resin and are not affected by the dissolution.

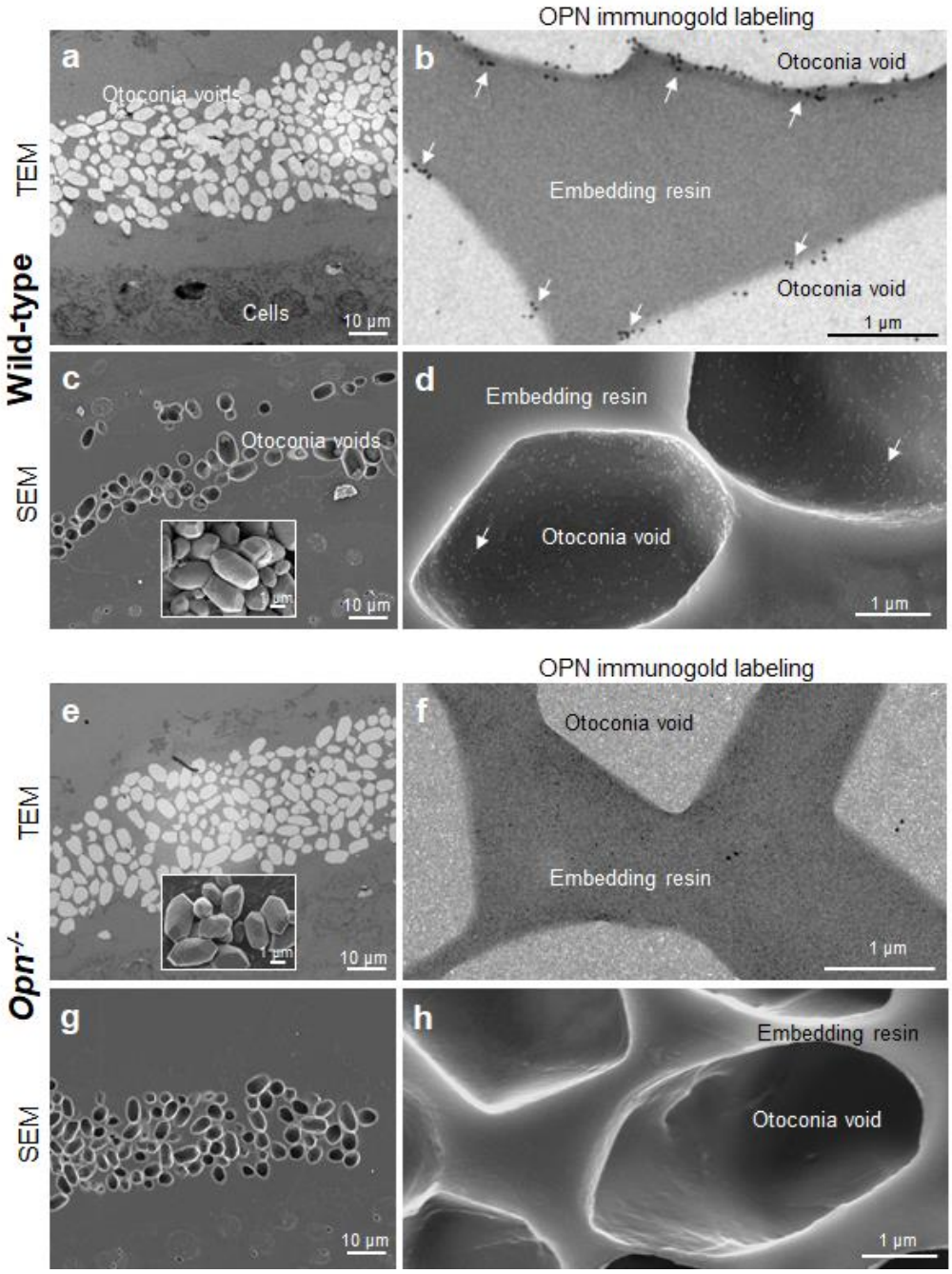

Figure 6. Immunogold labeling of OPN in otoconia. (a and c) In wild-type mice, otoconial voids shown by TEM and SEM, respectively, after immunolabeling for OPN (aqueous procedures dissolve the calcitic otoconia). Inset: Intact wild-type mouse otoconia (without aqueous exposure) shown by SEM. By TEM (b) and SEM (d), immunogold labeling for OPN shows gold particles (arrows) at the surface of otoconial voids. (e and g) In OPN-deficient mice, otoconial voids shown by TEM and SEM, respectively, after immunolabeling for OPN. Inset: Intact otoconia from OPN-deficient mice (without aqueous exposure) shown by SEM. By TEM (f) and SEM (h), as expected in this negative control, immunogold labeling for OPN was absent.

3.6 Effect of OPN on calcite crystal growth *in vitro*

To investigate a possible contribution of OPN protein to the production of nanostructure at the surface of otoconia, we examined the effects of OPN on calcite crystal growth *in vitro* as shown in Figure 6. At a low concentration of OPN (0.15 µM), calcite crystals retained their {104} rhombohedral morphology (Fig. 7a), but after increasing the OPN concentration to 0.3 µM and 0.45 µM, morphological changes became more evident to produce altered rounded growth step edges (Figs. 7b,c, respectively). At the highest OPN concentration used (0.9 µM), calcite crystals start developing aggregates of {104} rhombohedra (Fig. 6d), all with rough surfaces and apparent surface nanostructure similar to that seen at the surface of otoconia (Fig. 1c).

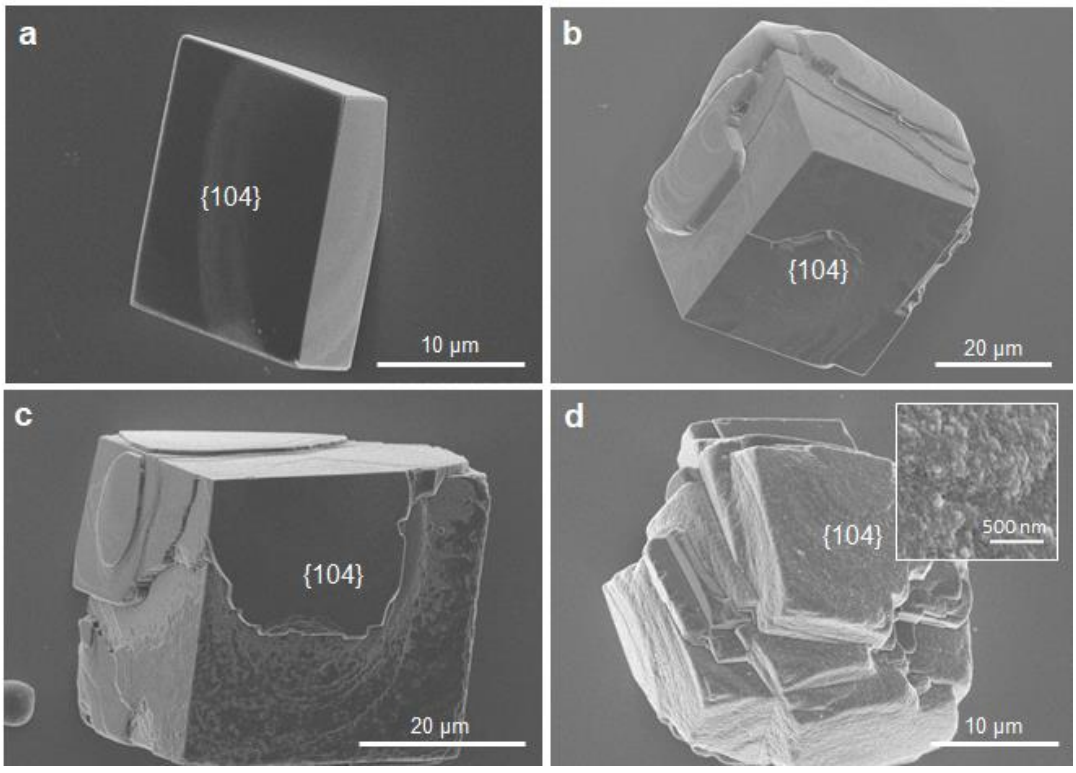

Figure 7. Effect of full-length purified OPN protein on calcite growth *in vitro*. Increasing concentration of OPN (a) 0.15 µM, (b) 0.3 µM, (c) 0.45 µM and (d) 0.9 µM gradually alters the external morphology of synthetically grown calcite crystals, producing evident surface nanostructure (inset).

4. Discussion

The structural and functional relationship between the organic matrix and the mineral component of various biomineralized tissues and structures – including otoconia – is a topic of considerable interest in the field of biomineralization. In recent years, reports on amorphous mineral phase precursors and mineral nanostructure have increasingly provided new insights into mechanistic processes for biomineralization at the molecular and atomic level. In biomineralized tissues and structures, mineral nanostructure has emerged as a common theme shared by many organisms where nanostructured morphology and mechanical properties can be attributed to the presence of incorporated organic matrix biomolecules (Wolf et al., 2016).

For calcitic mammalian otoconia – where in humans there exist major recognized debilitating health consequences linked to otoconial abnormalities and displacement – little is known about the structure of otoconia at the nanoscale. Using high-resolution, nanostructure-determining 2D and 3D characterization techniques, here we describe that there is an internal calcitic nanostructure in mouse otoconia consisting of domains approximately 50 nm in size with interwoven organic material surrounding individual inorganic calcitic nanostructures.

AFM in the tapping mode and using the phase function can discriminate between inorganic and organic phases within complex biomineral structures, being highly sensitive to sample inhomogeneity and compositional variations (Mass et al., 2014). Using this approach to study the interior of otoconia exposed by various means, we observed that the mineral phase consisted of closely packed and aligned nanogranules throughout the otoconial interior, a structural arrangement consistent with other descriptions of similar features in numerous calcareous biominerals such as, for example, the sea urchin spicule (Seto et al., 2012), mature tablets of nacre (Hovden et al., 2015), and chicken and guinea fowl eggshells (Athanasiadou et al., 2018; Perez-

Huerta and Dauphin, 2016). Commonly it seems in these cases, the nanogranules are aligned and surrounded by a fine organic matrix, or by a combination of organics and amorphous calcium carbonate (ACC) (Jean-Pierre Cuif, 2010). Notably, most observations on such biomineralized tissues/structures have revealed a nanostructure similar to what we report here for mammalian otoconia, this being roughly spheroidal fields of nanogranules ranging in size from between 50 to 100 nm (Perez-Huerta and Dauphin (Athanasiadou et al., 2018; Perez-Huerta and Dauphin, 2016). Such results are consistent with there being a nonclassical crystallization pathway to develop this nanostructure that deviates from the classical crystallization pathway (Rodriguez-Navarro et al., 2016; Wolf et al., 2016), but additional work under cryo-conditions is needed to confirm this. Previous model studies have indicated that organic additives, *e.g*. acidic biomacromolecules, could favor a nonclassical aggregation-based crystal growth mechanism by stabilizing ACC particles (Cölfen, 2008; Wolf et al., 2016). In the present study in 8-day-old mice, ACC was not detected in the otoconia from the Ca-K edge XAS and Raman spectroscopy, but this could be attributed to its loss during sample preparation, or to the relatively mature state of the examined otoconia, where ACC could in fact be present at earlier prenatal or perinatal developmental stages of mouse otoconial development.

The smallest nanodomain size that we observed in the otoconia was approximately 10 nm, as observed by HRTEM. Differences in these dimensions could be related to regional variations in organic content (likely type or amount of proteins) acting as inhibitors/regulators of mineralization as has been proposed for the calcitic nanostructure of chicken eggshell *G. gallus domesticus* (Athanasiadou et al., 2018). Previously, *in vitro* crystal growth work by others has shown that OC90, fetuin-A and OPN act as inhibitors of calcite crystal growth, primarily attributable to their having high-binding affinity to calcium (Hong et al., 2015). These results are

in agreement with our own calcite crystal growth experiments in which the presence of OPN modifies the typical rhombohedral shape of calcite in a concentration-dependent manner. With increasing OPN concentration, the {104} crystal faces of calcite have abundant growth islands and rounded step edges, and evident surface nanostructure, disclosing changes in the growth mechanism of these crystal faces attributable to the added OPN. Even at higher OPN concentrations, the synthetic calcite crystals tend to create aggregates with rough surfaces of slightly mismatched {104} rhombohedra. Although this reflects surface activity, we previously have shown that beyond the surface, additional incorporation of OPN occurs into the crystal interior to generate internal nanostructure (Athanasiadou et al., 2018).

In previous *in vitro* calcite growth experiments by others, it was shown that the addition of either OC90 or otolin protein alone could not produce the external shape of mature otoconia, but when both proteins were added in combination, they could to some degree produce calcitic structures that resembled otoconial morphology (Moreland et al., 2014). Similar to this, calcite-gelatin composites grown by a double-diffusion method in gelatin gel matrices revealed similar morphological features to mammalian otoconia (having branch and belly regions), but these were much larger in size (Huang et al., 2008). Focused-ion beam-cut sections of these artificial composites demonstrated a dense crystalline branch region and a poorly crystalline belly region (Simon et al., 2011).

Occluded OPN into synthetic calcite crystals can induce a nanostructure similar to the nanostructure observed in calcitic chicken eggshell, where higher OPN concentration creates smaller nanostructure and increases hardness (Athanasiadou et al., 2018). Our finding showing that OPN is concentrated at the surface of the otoconia as detected by high-resolution, postembedding immunogold labeling is novel at the ultrastructural level, and is consistent with

previous studies using conventional immunohistochemistry and light microscopy (Sakagami, 2000; Takemura et al., 1994). However, because otoconial calcite is readily soluble under aqueous conditions, dissolution of the mineral rapidly occurs during the required aqueous immunolabeling incubation and washing steps, and we were not able to associate OPN with interior structure (only with the surface region where the embedding medium retained resident components). Thus, while likely affecting surface mineralization of the otoconia, it remains possible that OPN is also present within the interior of otoconia and contributes to the nanostructure that we have observed here, and which can be reproduced *in vitro* using OPN. Indeed, otoconins such as OC90 could likewise participate in this nanostructuring process. OPN is co-expressed locally in the inner ear with OC90 by the vestibular dark cells and in the endolymphatic sac (Ignatova et al., 2004; Sakagami, 2000; Verpy et al., 1999), meaning that OC90 and OPN could have similar functions in some regard, even partially compensating for each other during otoconial formation. In particular, OC90 has a strong effect on otoconial formation; OC90-knockout mice have rodlike large calcitic aggregates that are susceptible to dissolution (Zhao et al., 2007). In contrast, in OPN-null mice where Oc90 levels are presumably not altered, there is normal balance behavior and normal otoconial morphology (Zhao et al., 2008). Since OPN has now been localized to the very periphery of otoconia in mice (our work) and in rats (Takemura et al., 1994), and given its role in creating mineral nanotexture as we have recently shown for calcite crystals in the chicken eggshell, OPN could indeed be a protein involved in controlling surface growth and nanostructure in otoconia. However, the interplay between OPN and OC90, if any, along with interactions amongst other otoconial proteins in this biomineralization process, remains to be determined.

5. Conclusions

In summary, the internal structure of mouse otoconia at the nanoscale has been determined. Within the interior of otoconia, using a combination of advanced imaging techniques, we show that otoconia consist of densely packed calcite nanodomains surrounded by organic material, with OPN being present at the very surface of the otoconia. The surface localization of OPN suggests involvement in the growth process and/or termination of otoconial growth via the mineralization-inhibiting activity of this protein on crystal growth. This study provides detailed findings on the internal and external structure of otoconia, information that may lead to a better understanding of what goes wrong with otoconia in diseases such as vertigo.

Acknowledgments

We are grateful to Ms. Lydia Malynowsky and Dr. Betty Hoac for otoconia dissections. We also thank Dr. Kelly Sears, Dr. David Liu, Ms. Weawkamol Leelapornpisit, Dr. Kaustuv Basu and Prof. Khanh Huy Bui for assistance with FIB, TEM and tomography work, and Dr. Rui Tahara for assistance with Xradia 520 Versa imaging. We would like also to thank the Soft X-ray Microcharacterization Beamline (SXRMB) 06B1-1 at the Canadian Light Source (CLS) for their technical support, and the Canadian Light Source (CLS) for financial travel support. We also gratefully thanks Dr. Nicole Hondow and Dr. Zabeada Aslam of the Leeds Electron Microscopy and Spectroscopy Centre. This work was supported by Canadian Institutes of Health Research (MOP-142330) and the Natural Sciences and Engineering Research Council of Canada (RGPIN-2016-05031) to MDM. MDM is a member of the FRQ-S Network for Oral and Bone Health Research. This research was undertaken, in part, thanks to funding from the Canada Research Chairs program.

6. Supplementary Material

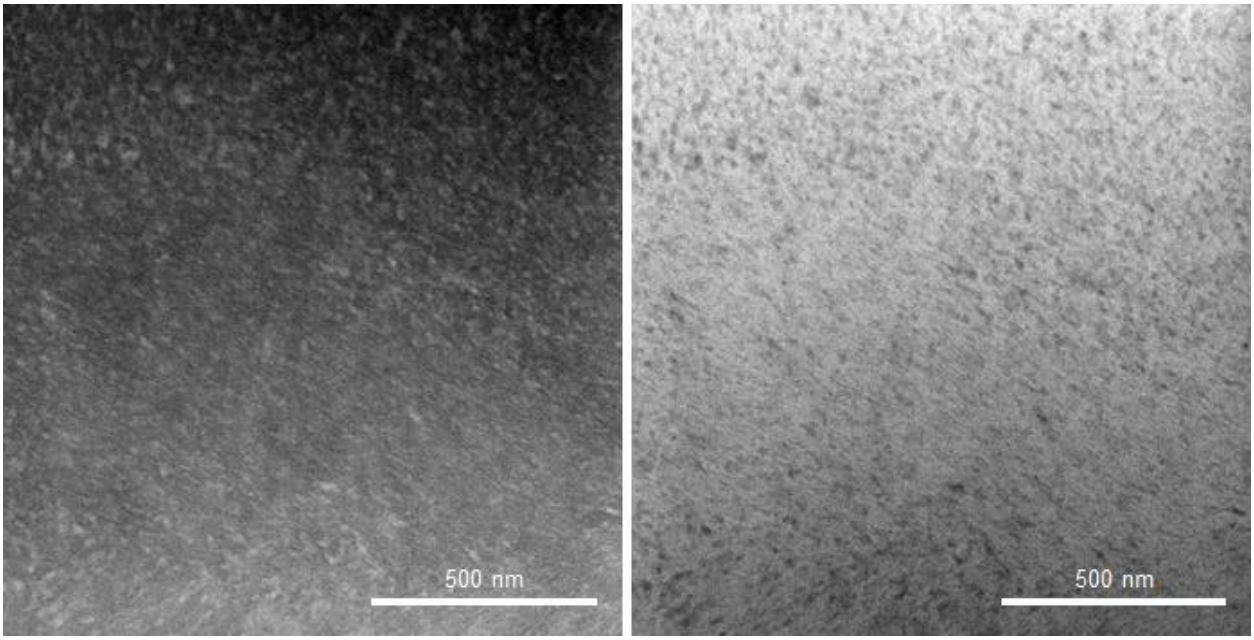

Fig. S1 Otoconia nanostructure observed by STEM. (a) Bright-field and (b) HAADF TEM images from a STEM tilt series where nanostructure is clearly evident.

Movie S1. Three-dimensional reconstruction of utricular otoconia (otoconia in grey, and bone in orange) from an X-ray computed tomography series.

Movie S2. Three-dimensional reconstruction from the branch region of an 8-day-old mouse utricular otoconium from a TEM tomography tilt series.

Movie S3. Three-dimensional reconstruction by solid- and surface-rendering of a nanostructured area from the branch region of an 8-day-old mouse utricular otoconium from a TEM tomography tilt series.

References

Addadi, L., et al. 2003. Taking advantage of disorder: amorphous calcium carbonate and its roles in biomineralization. Adv. Mater. 15, 959-970.

Agrawal, Y., et al. 2009. Disorders of balance and vestibular function in us adults: data from the national health and nutrition examination survey, 2001-2004. Arch. Intern. Med. 169, 1419-1419.

Andrade, L.R., et al. 2012. Immunogold TEM of otoconin 90 and otolin - relevance to mineralization of otoconia, and pathogenesis of benign positional vertigo. Hear. Res. 292, 14-25.

Anniko, M., et al. 1984. Microprobe analysis of human otoconia. Acta Oto-Laryngol. 97, 283-289.

Athanasiadou, D., et al. 2018. Nanostructure, osteopontin, and mechanical properties of calcitic avian eggshell. Sci. Adv. 4, eaar3219.

Carlstrom, D.D., 1963. Crystallographic study of vertebrate otoliths. Biol. Bull. 125, 441-463.

Cölfen, H., Antonietti, M., 2008. Mesocrystals and nonclassical crystallization. John Wiley & Sons, Ltd.

De Yoreo, J.J., et al. 2015. Crystal growth. Crystallization by particle attachment in synthetic, biogenic, and geologic environments. Science 349, aaa6760.

Fermin, C.D., et al. 1995. The glycan keratan sulfate in inner ear crystals. Cell Mol. Biol. 41, 577-591.

Fisher, L.W., et al. 2001. Flexible structures of SIBLING proteins, bone sialoprotein, and osteopontin. Biochem. Bioph. Res. Comm. 280, 460-465.

Hiatt, G.A., 2014. Color atlas and text of histology. Wolters Kluwer.

Hong, M.N., et al. 2015. Effect of otoconial proteins fetuin a, osteopontin, and otoconin 90 on the nucleation and growth of calcite. Cryst. Growth Des. 15, 129-136.

House, M.G., Honrubia, V., 2003. Theoretical models for the mechanisms of benign paroxysmal positional vertigo. Audiol. Neurotol. 8, 91-99.

Hovden, R., et al. 2015. Nanoscale assembly processes revealed in the nacroprismatic transition zone of Pinna nobilis mollusc shells. Nat. Commun. 6, 1-7.

Huang, Y.X., et al. 2008. Shape development and structure of a complex (otoconia-like?) calcite-gelatine composite. Angew. Chem. Int. 47, 8280-8284.

Hughes, I., et al. 2006. Mixing model systems: using zebrafish and mouse inner ear mutants and other organ systems to unravel the mystery of otoconial development. Brain Res. 1091, 58-74.

Ignatova, E.G., et al. 2004. Molecular mechanisms underlying ectopic otoconia-like particles in the endolymphatic sac of embryonic mice. Hear. Res. 194, 65-72.

Cuif, J.-P., et al. 2010. Biominerals and fossils through time. Cambridge university press, Cambridge.

Johnsson, L.G., et al. 1982. Pathology of neuroepithelial suprastructures of the human inner-ear. Am. J. Otolaryngol. 3, 77-90.

Kremer, J.R., et al. 1996. Computer visualization of three-dimensional image data using IMOD. J. Struct. Biol. 116, 71-76.

Lins, U., et al. 2000. The otoconia of the guinea pig utricle: internal structure, surface exposure, and interactions with the filament matrix. J. Struct. Biol. 131, 67-78.

Lowenstam, H.A., Weiner, S., 1989. On biomineralization. Oxford university press, New York.

Lu, W., et al. 2010. In vitro effects of recombinant otoconin 90 upon calcite crystal growth. Significance of tertiary structure. Hear. Res. 268, 172-183.

599 Lundberg, Y.W., Xu, Y., 2012. Proteins involved in otoconia formation and maintenance, in:
600 Gendeh, B.S., (Ed.), Otolaryngology, InTech, pp. 1-22.
601 Lundberg, Y.W., et al. 2015. Mechanisms of otoconia and otolith development. Dev. Dynam. 244,
602 239-253.
603 Marieb, E.N., 1991. Essentials of human anatomy and physiology, Essentials of human anatomy
604 and physiology.
605 Mass, T., et al. 2014. Immunolocalization of skeletal matrix proteins in tissue and mineral of the
606 coral Stylophora pistillata. Proc. Natl. Acad. Sci. USA 111, 12728-12733.
607 Moreland, K.T., et al. 2014. In vitro calcite crystal morphology is modulated by otoconial proteins
608 otolin-1 and otoconin-90. Plos One 9, e95333.
609 Murayama, E., et al. 2005. Otolith matrix proteins OMP-1 and Otolin-1 are necessary for normal
610 otolith growth and their correct anchoring onto the sensory maculae. Mech. Develop. 122,
611 791-803.
612 Oas, J.G., 2001. Benign paroxysmal positional vertigo: a clinician's perspective. Ann. N. Y. Acad.
613 Sci. 942, 201-209.
614 Ornitz, D.M., et al. 1998. Otoconial agenesis in tilted mutant mice. Hear. Res. 122, 60-70.
615 Perez-Huerta, A., Dauphin, Y., 2016. Comparison of the structure, crystallography and
616 composition of eggshells of the guinea fowl and graylag goose. Zoology. 119, 52-63.
617 Politi, Y., et al. 2006. Structural characterization of the transient amorphous calcium carbonate
618 precursor phase in sea urchin embryos. Adv. Funct. Mater. 16, 1289-1298.
619 Pote, K.G., Ross, M.D., 1986. Ultrastructural morphology and protein-content of the internal
620 organic material of rat otoconia. J. Ultra. Mol. Struct. Res. 95, 61-70.
621 Pote, K.G., Ross, M.D., 1991. Each otoconia polymorph has a protein unique to that polymorph.
622 Comp. Biochem. Phys. B 98, 287-295.
623 Pote, K.G., Ross, M.D., 1993. Utricular otoconia of some amphibians have calcitic morphology.
624 Hear. Res. 67, 189-197.
625 Rodriguez-Navarro, C., et al. 2016. Nonclassical crystallization in vivo et in vitro (II):
626 nanogranular features in biomimetic minerals disclose a general colloid-mediated crystal
627 growth mechanism. J. Struct. Biol. 196, 260-287.
628 Ross, M.D., Pote, K.G., 1984. Some properties of otoconia. Philos. T. Roy. Soc. B 304, 445-452.
629 Sakagami, M., 2000. Role of osteopontin in the rodent inner ear as revealed by in situ
630 hybridization. Med. Electron Microsc. 33, 3-10.
631 Salvinelli, F., et al. 2004. Benign paroxysmal positional vertigo: diagnosis and treatment. Clin.
632 Ter. 155, 395-400.
633 Seto, J., et al. 2012. Structure-property relationships of a biological mesocrystal in the adult sea
634 urchin spine. Proc. Natl. Acad. Sci. USA 109, 7126-7132.
635 Simon, P., et al. 2011. Structural relationship between calcite-gelatine composites and biogenic
636 (human) otoconia. Eur. J. Inorg. Chem. 5370-5377.
637 Sodek, J., et al. 2000. Osteopontin. Crit. Rev. Oral Biol. M 11, 279-303.
638 Sorensen, E.S., Petersen, T.E., 1993. Purification and characterization of 3 proteins isolated from
639 the proteose peptone fraction of bovine-milk. J. Dairy Res. 60, 189-197.
640 Sorensen, E.S., et al. 1995. Posttranslational modifications of bovine osteopontin: identification of
641 twenty-eight phosphorylation and three O-glycosylation sites. Protein Sci. 4, 2040-2049.
642 Tachibana, M., Morioka, H., 1992. Glucuronic acid-containing glycosaminoglycans occur in
643 otoconia: cytochemical evidence by hyaluronidase-gold labeling. Hear. Res. 62, 11-15.

644 Takemura, T., et al. 1994. Localization of osteopontin in the otoconial organs of adult rats. Hear.
645 Res. 79, 99-104.
646 Thalmann, I., et al. 2006. Microscale analysis of proteins in inner ear tissues and fluids with
647 emphasis on endolymphatic sac, otoconia, and organ of Corti. Electrophoresis 27, 1598-
648 1608.
649 Tseng, Y.H., et al. 2014. $CaCO_3$ nanostructured crystals induced by nacreous organic extracts.
650 Cryst. Eng. Comm. 16, 561-569.
651 Verpy, E., et al. 1999. Characterization of otoconin-95, the major protein of murine otoconia,
652 provides insights into the formation of these inner ear biominerals. Proc. Natl. Acad. Sci.
653 USA 96, 529-534.
654 Vibert, D., et al. 2003. Benign paroxysmal positional vertigo in older women may be related to
655 osteoporosis and osteopenia. Ann. Oto. Rhinol. Laryn. 112, 885-889.
656 Walther, L.E., et al. 2014. The inner structure of human otoconia. Otol. Neurotol. 35, 686-694.
657 Wehrmeister, U., et al. 2011. Amorphous, nanocrystalline and crystalline calcium carbonates in
658 biological materials. J. Raman Spectrosc. 42, 926-935.
659 Wolf, S.E., et al. 2016. Nonclassical crystallization in vivo et in vitro (I): process-structure-
660 property relationships of nanogranular biominerals. J. Struct. Biol. 196, 244-259.
661 Wright, C.G., et al. 1982. A calcareous concretion in the posterior semicircular duct of a human
662 labyrinth. Am. J. Otolarynogol. 3, 196-201.
663 Xu, Y., et al. 2010. Expression, functional, and structural analysis of proteins critical for otoconia
664 development. Dev. Dyn. 239, 2659-2673.
665 Yang, H., et al. 2011. Matrix recruitment and calcium sequestration for spatial specific otoconia
666 development. Plos One 6, e20498.
667 Zhao, X., et al. 2007. Gene targeting reveals the role of Oc90 as the essential organizer of the
668 otoconial organic matrix. Dev. Biol. 304, 508-524.
669 Zhao, X., et al. 2008. Osteopontin is not critical for otoconia formation or balance function. J.
670 Assoc. Res. Otolaryngol. 9, 191-201.

671